remote sensing

MDPI

Article

Enhancement of Cloudless Skies Frequency over a Large Tropical Reservoir in Brazil

André R. Gonçalves [1,*], Arcilan T. Assireu [2], Fernando R. Martins [3], Madeleine S. G. Casagrande [3], Enrique V. Mattos [2], Rodrigo S. Costa [1], Robson B. Passos [2], Silvia V. Pereira [1], Marcelo P. Pes [1], Francisco J. L. Lima [1] and Enio B. Pereira [1]

1 National Institute for Space Research, Av. dos Astronautas, 1758, São José dos Campos SP 12227-010, Brazil; rodrigo.costa@inpe.br (R.S.C.); silvia.pereira@inpe.br (S.V.P.); marcelo.pes@inpe.br (M.P.P.); francisco.lopes@inpe.br (F.J.L.L.); enio.pereira@inpe.br (E.B.P.)

2 Federal University of Itajuba, Av. BPS, 1303, Pinheirinho, Itajubá MG 37500-903, Brazil; arcilan@unifei.edu.br (A.T.A.); enrique@unifei.edu.br (E.V.M.); robsonbarretodospassos@gmail.com (R.B.P.)

3 Federal University of São Paulo, Rua Carvalho de Mendonça, 144, Santos SP 11070-102, Brazil; fernando.martins@unifesp.br (F.R.M.); madeleine.gacita@unifesp.br (M.S.G.C.)

* Correspondence: andre.goncalves@inpe.br; Tel.: +55-12-3208-7908

Received: 20 July 2020; Accepted: 25 August 2020; Published: 27 August 2020

Abstract: Several studies show the effects of lake breezes on cloudiness over natural lakes and large rivers, but only few contain information regarding large flooded areas of hydroelectric dams. Most Brazilian hydropower plants have large water reservoirs that may induce significant changes in the local environment. In this work, we describe the prevailing breeze mechanism in a Brazilian tropical hydropower reservoir to assess its impacts on local cloudiness and incoming surface solar irradiation. GOES-16 visible imagery, ISCCP database products, and ground measurement sites operated by INMET and LABREN/INPE provided data for the statistical analysis. We evaluate the cloudiness frequency assuming two distinct perspectives: spatial distribution by comparing cloudiness over the water surface and areas nearby its shores, and time analysis by comparing cloudiness prior and after reservoir completion. We also evaluated the solar irradiance enhancement over the water surface compared to the border and land areas surrounding the hydropower reservoir. The results pointed out daily average cloudiness increases moving away from the reservoir in any of the four cardinal directions. When looking at the afternoon-only cloudiness (14h to 16h local time), 4% fewer clouds were observed over the flooded area during summer (DJF). This difference reaches 8% during autumn (MAM) and spring (SON). Consequently, the irradiance enhancement at the water surface compared to external areas was around 1.75% for daily average and 4.59% for the afternoon-only average. Our results suggest that floating solar PV power plants in hydropower reservoirs can be an excellent option to integrate both renewable energy resources into a hybrid power generation due to the high solar irradiance in Brazilian territory combined with the prevailing breeze mechanism in large tropical water reservoirs.

Keywords: lake breeze influence; hydropower reservoir; solar irradiance enhancement; solar energy resource

1. Introduction

Lake breeze circulation is one of the most well-known thermally-induced phenomena in mesoscale meteorology. The onset of a lake breeze depends on the ratio between the thermal to inertial driving forces, as discussed by Biggs and Graves [1]. Despite the well-described physical mechanism, the evaluation of its occurrence and strength is not a simple task due to surface heterogeneity, terrain effects, and synoptic patterns superimposed on the flow.

Rabin et al. [2] compared the surface heterogeneity (based on the Normalized Difference Vegetation Index (NDVI) data) with the Geostationary Operational Environmental Satellite (GOES) visible imagery and reported cloud-free bands downwind during the warm season over large lakes in the USA. Several other studies investigated the characteristics of lake breezes on the temperate and subtropical region. Segal et al. [3] evaluated the lake breeze phenomena in Florida (USA) using modeling and observational approaches. They reported that the atmospheric forcing induced by subsidence and suppression of the cumulus cloud mutually contribute to the increase in the cloudless frequency over the lakes. Asefi-Najafabady et al. [4] used the dual-Doppler radar to analyze 3-D flows induced by an elongated 2 km wide reservoir in Alabama (USA) during summer. The horizontal scale of the breeze circulation was approximately 10 km in both shores but was extremely sensitive to wind speed changes and direction. The authors mentioned a simultaneously cloud-free zone over the lake observed from GOES satellite. Iakunin et al. [5] have shown that the lake breeze for the Alqueva reservoir (southeast of Portugal) could be detected at a distance of more than 6 km away from the shores and at altitudes up to 300 m above the water surface based on observation and model. Crosman and Horel [6] published an extensive review of numerical studies on lake breeze dynamics providing a significant contribution to the understanding of this phenomenon. It is a consensus among researchers that factors like the sensible heat flux, synoptic wind, atmospheric stability, watershed dimensions, terrain slope, and roughness affect lake breeze occurrence.

Enhanced potential for breeze production is expected in tropical regions due to higher evapotranspiration and heat availability. For example, in the Amazon rainforest, the evapotranspiration is intense and exerts a notable influence on regional and global climate patterns, playing a significant role in cloudiness observed over large rivers and the water balance [7]. Silva Dias et al. [8] reported such an effect by studying the atmospheric circulation induced by the Tapajós River. They observed that this circulation causes the formation of shallow cumulus during the morning hours over the eastern riverside and suppresses cloud formation in the western riverside during the afternoon. Yin et al. [9] analyzed the daily cycle of cloudiness over Lake Victoria (East Africa) and its influence on lake evaporation. The authors concluded that the cloudiness varies up to 22% between day and night in the northeastern quadrant of the lake, but it varied seasonally throughout the year.

This phenomenon is not constrained to large natural lakes and rivers, as it affects large flooded areas such as hydroelectric dams. The formation of large water reservoirs to feed large hydropower plants in tropical regions may present a similar pattern of lake breeze [5,10–14]. Most Brazilian hydroelectric plants have large water reservoirs that eventually lead to lake breezes and induce extensive changes in the local environment. The replacement of the land cover by the water reservoirs causes intense thermal gradients between the flooded area and the surrounding territory that may trigger lake breeze circulations and impacts the hydrological cycle, energy balance, local cloudiness, and economic activities such as agriculture and tourism. Stivari et al. [10,15] showed that lake breeze circulation is a dominant feature in the local climate on the Lake Itaipu, the water reservoir of the Itaipu Brazil-Paraguay hydropower plant. According to these studies, the water surface is consistently colder than the land in lake borders with a thermal contrast up to −3 °C during the daytime. The lake is systematically warmer at night, presenting a thermal contrast of up to +8 °C. This thermal contrast could trigger the lake breeze circulation and, thus, inhibit the formation of shallow clouds during the day. However, to the best of our knowledge, the occurrence of this phenomenon in artificial tropical hydroelectric reservoirs and its characterization have not yet been addressed. In this way, the objective of this study is to investigate the formation of the lake breeze and the magnitude and spatial pattern of enhanced cloudless skies over a tropical reservoir in Brazil.

In this work, we describe the prevailing breeze mechanism in the artificial lake of a Brazilian hydroelectric plant in the tropical region. We investigate its impact on cloudless skies frequency and incoming surface solar irradiation based on observational data and statistical metrics. We evaluate the cloudiness frequency using two different approaches: spatial distribution by comparing cloudiness over the reservoir and in the areas nearby its shores, and time analysis by comparing cloudiness prior

and after reservoir completion. Our results can provide information to foster the use of solar energy resources in hydroelectric dams of tropical regions through the technology of floating photovoltaics. Solar-hydro hybrid plants can become a great alternative to integrate both resources due to the high solar irradiance in the Brazilian territory combined with the breeze mechanism produced by many dams.

2. Materials and Methods

2.1. Water Reservoir Description

The target area for this study is the Serra da Mesa hydropower plant (14°00′ S, 48°21′ W), located in a stretched region between the states of Goiás and Tocantins (central region of Brazil) as illustrated in Figure 1.

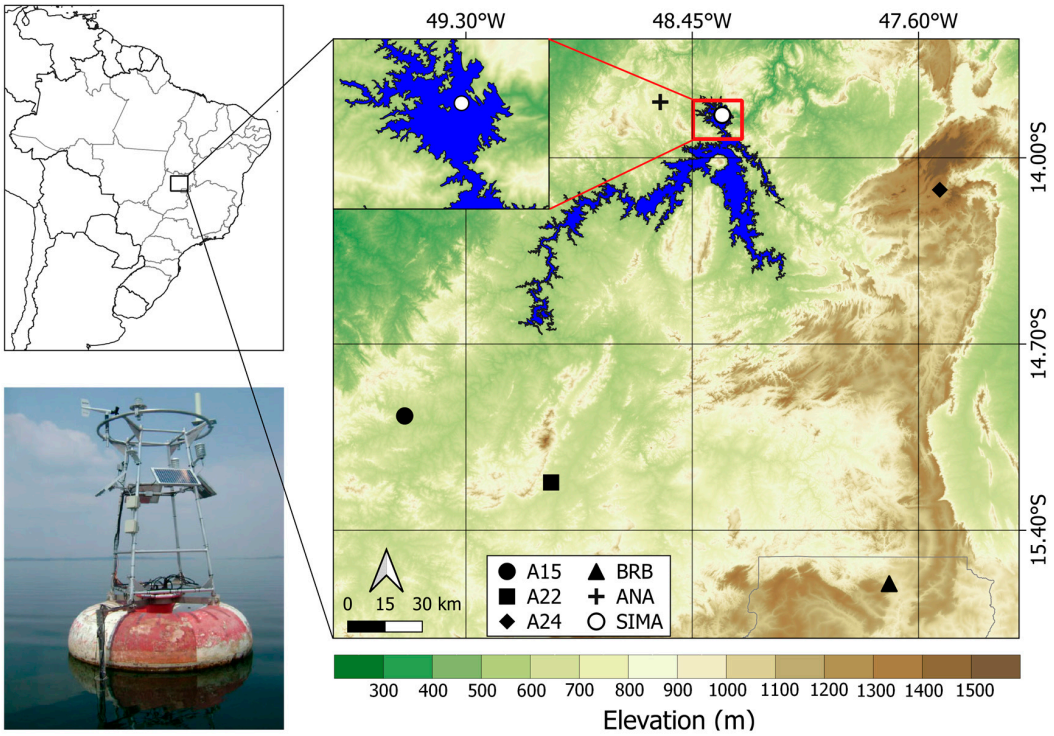

Figure 1. The geographical location of the Serra da Mesa water reservoir in the Central region of Brazil the lake geography, the locations of the ground stations and a picture of SIMA autonomous data collection buoy system in operation in the northern area of the lake.

The power plant has an installed capacity of 1275 MW, and its reservoir was established in 1998 in a region that was originally covered with tropical grassland savanna. Due to the basin's geomorphology, which is based on rugged terrain in the transition between Brazilian central elevated plains and Amazon basin lowlands, the lake presents a dendritic pattern covering a surface area of approximately 1784 km^2, with the maximum depth ~150 m. The reservoir's width is up to 8 km in the most extended portions, and the total water volume is ~54.4 billion m^3. The elevation along the nearby Tocantins River ranges from a minimum of 340 m above MSL (mean sea level) to 1100 m in the highest ridges. The regional climate is categorized as Aw–Tropical Savannah by Köppen-Geiger climate classification [16], with dry winter and rainy season occurring from November to March summing up to 1600 mm of precipitation per year [17]. The rainfall is modulated by the South American Monsoon System [18] with significant influence of other atmospheric systems such as cold fronts and squall lines. Winds are usually calm (2–3 m/s), and the monthly average temperature remains between 20 °C and 28 °C throughout the year [17].

2.2. Datasets Description

This study uses three sources of data to assess lake breeze impact on cloudiness: in situ measurements (5 years), a high-resolution short-term satellite dataset (one year), and a low-resolution long-term satellite dataset (29 years). Each of the datasets delivers complementary information on the breeze characteristics and impact from a climatological perspective. A flowchart describing the whole analysis is presented in Figure 2.

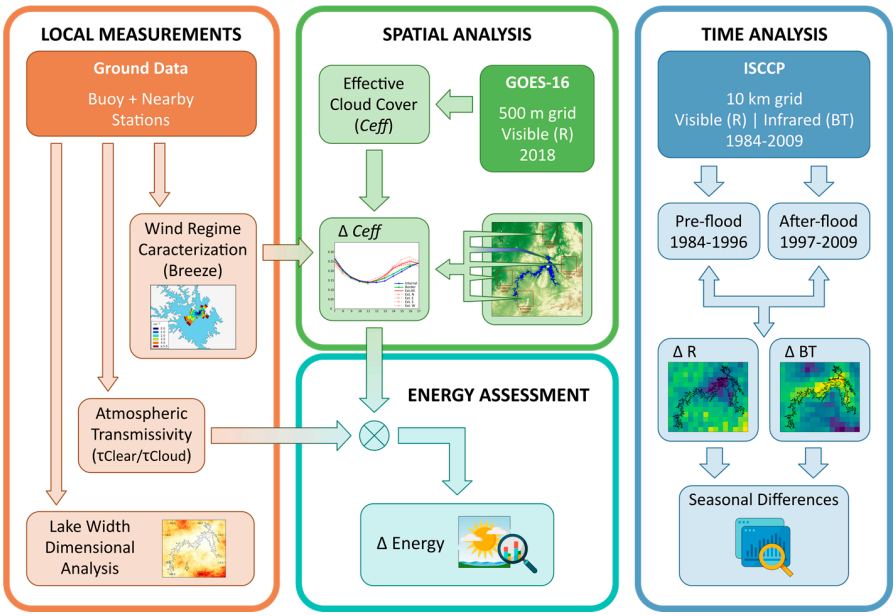

Figure 2. Flowchart of the three strategies used in this study to characterize the lake breeze: in situ measurements (5 years), a high-resolution short-term satellite dataset (one year), and a low-resolution long-term satellite dataset (29 years).

2.2.1. Ground-Based Dataset

Figure 1 shows the location of the buoy-based system for environmental monitoring (SIMA, a Brazilian Portuguese acronym) used for meteorological data acquisition, including air temperature, humidity, air pressure, wind intensity, and water temperature at 2, 5, 20, and 40 m depth. The buoy is anchored by cables attached to two train wheels, which guarantees a fixed geographic position. The observational data comprises hourly records from 2005 to 2010. The 10-min average wind data was recorded at hourly intervals. Table 1 summarizes the sensors and their technical specifications.

Table 1. Technical specifications of the sensors used in the SIMA buoy operating in the Serra da Mesa Reservoir. Adapted from Stech et al. [19].

Sensor	Manufacture	Range	Accuracy	Depth/Height
Air Temperature	Rotronic	−25 to 60 °C	±0.3 °C	3 m
Water Temperature	Yellow Spring	−5 to 60 °C	±0.15 °C	−2, −5, −20, −40 m
Wind Speed *	R.M. Young	0 to 100 ms^{-1}	±0.3 ms^{-1}	3 m
Wind Direction	R.M. Young	0 to 360°	±3°	3 m
Relative Humidity	Rotronic	0 to 100%	±1.5%	3 m
Barometric Pressure	Vaisala	500 to 1100 hPa	±0.3 hPa	3 m

* Wind direction is measured by combining the apparent wind direction from the anemometer vane and the orientation of the buoy from a compass.

Four other ground stations were used for regional estimates of climate-relevant variables for this study, such as ambient wind (10-m) and clear-sky transmissivity (through global horizontal irradiance,

GHI). These stations are operated by the SONDA project at from the National Institute for Space Research (INPE) and by the Brazilian National Meteorological Institute (INMET). Table 2 describes these data in more detail, including the SIMA buoy presented in Table 1.

Table 2. Details of SIMA buoy system and ground measurement sites near the Serra da Mesa Reservoir used to estimate the climate-relevant variables for this study.

Met. Station	Operated by	Distance to Shore (km)	Lat (°)	Lon (°)	Alt (m)	Period and Resolution	Variables Used
SIMA	INPE	offshore	−13.84	−48.33	476	2005–2010 Hourly	Table 1
ANA	ANA	15	−13.79	−48.57	694	1971–2018 Daily	Precipitation
BRB	INPE	140	−15.60	−47.71	1023	2005–2018 Minute	GHI
A15	INMET	64	−14.97	−49.53	522	2007–2018 Hourly	Wind
A22	INMET	76	−15.22	−48.98	667	2007–2018 Hourly	GHI, Wind
A24	INMET	63	−14.12	−47.52	1260	2007–2018 Hourly	GHI, Wind

2.2.2. Satellite-Based Datasets

In addition to the ground data, two satellite-derived datasets were used to evaluate the spatial and time distributions of cloudiness: the visible imagery of South America acquired by GOES−16 satellite and the Gridded Satellite images (GridSat-B1).

The National Oceanic and Atmospheric Administration (NOAA) operates the geostationary satellite GOES-16 over the Equator at 75.2° West and provides access to its visible imagery databases [20]. We used the 'RED' band images (Channel 2—central wavelength at 0.64 µm) to identify small-scale features such as river fogs and fog/clear air boundary images due to the 0.5 km spatial resolution (at the sub-satellite point). Images from the year of 2018 at one-hour intervals and native spherical grid resolution provided a highly detailed cloud pattern diagnosis over the reservoir and its shores. Despite sub-hourly imagery availability for GOES-16 in 2018, the hourly images create a satisfactory sample for cloudiness characterization.

Cloud detection from GOES-16 visible channel (0.64 µm) is impaired by surface brightness. A strategy to overcome this obstacle is to employ the Effective Cloud Cover (C_{eff}) index as a proxy for cloud coverage, as proposed in Equation (1) by Moser and Raschke [21]

$$C_{eff} = \frac{R - R_{min}}{R_{máx} - R_{min}} \quad (1)$$

where R is the visible reflectance acquired by GOES-16 at a particular pixel, and R_{min} and $R_{máx}$ are, respectively, the reflectance for cloudless and overcast sky condition. R_{min} is estimated based on a statistical analysis of satellite data observed over the same pixel in one month and is hourly dependent due to surface anisotropy effects. On the other hand, $R_{máx}$ is the maximum visible reflectance normalized by the solar zenith angle.

C_{eff} is a dimensionless coefficient, and it can assume values from zero (cloudless condition) to one (optically very thick cloudiness condition). It accounts for surface reflectivity, allowing detection of shallow cumulus clouds, typically formed in breeze fronts at the shorelines. In addition, C_{eff} has an almost linear relationship with the transmittance of solar radiation through clouds, providing a way to estimate the solar radiation incident on the surface [22]. Hourly data from the GOES-16 satellite were processed to get the C_{eff} values required to evaluate the lake breeze influence on cloudiness, and therefore the incoming solar irradiance at the surface.

The World Climate Research Program developed and delivered the second gridded satellite database (GridSat-B1) [23]. It is based on the ISCCP-B1 product of the International Satellite Cloud Climatology Project (ISCCP) [24], focusing on the global distribution of cloudiness, cloud properties, and seasonal variability. The GridSat-B1 database is gridded on a 0.07-degree surface resolution and comprises merged data by selecting the nadir-most satellite observations for each grid point. The GridSat-B1 encompasses data from three spectral band channels: infrared (around 11.0 µm), water

vapor (around 6.7 µm), and visible (around 0.65 µm). The database comprises cloudiness data from 1984 to 2009 with 3-hr time resolution, allowing an assessment before and after reservoir flooding.

The infrared brightness temperature (BT) and visible reflectance (R) were proxies for cloudiness occurrence. BT is related to the energy emitted from cloud tops. In contrast, R represents the reflected solar energy from cloud tops. High clouds have low BT [25], while high R values are associated with clouds of high optical thickness. Only image pixels presenting BT lower than 0 °C (~4 km above the Mean Sea Level) were considered to minimize the effects of surface radiation contamination according to studies on cloud classification by Rossow and Garder [26] and Bottino and Ceballos [27].

The long-term database (29 years) of satellite data allows a comparison analysis of cloudiness occurrence before (1984–1996) and after (1997–2009) the Serra da Mesa reservoir construction. The difference between the observed BT "after" and "before" was assessed for the Serra da Mesa hydropower area, including the flooded and surrounding areas. The positive difference between the BT values indicates shallower clouds or less cloud occurrence. A similar procedure was adopted using reflectance data. The signal of the difference between the reflectance values "after" and "before" indicates an increase (+) or decrease (−) in the cloud optical thickness or clouds occurrence frequency.

The Kolmogorov–Smirnov two-sample homogeneity test (K–S test) was applied to prevent any misleading conclusion on the time series of cloudiness before and after filling the Serra da Mesa reservoir. This nonparametric test allows inferring, at a certain significance level (α), if two datasets have the same cumulative frequency distribution (CDF). The statistic parameter D_n is the maximum absolute differences between two CDFs, as shown in Equation (2):

$$D_n = \max\left(\left|F(x) - R(x)\right|\right) \tag{2}$$

where $R(x)$ is the reference cumulative distribution function, and $F(x)$ is the tested distribution. The K–S test rejects the null hypothesis if D_n is not within critical bounds V_c given in Equation (3) for $\alpha = 0.01$.

$$V_c = 1.63 \cdot \sqrt{\frac{n1 + n2}{n1 \cdot n2}} \tag{3}$$

where $n1$ and $n2$ are the sizes of the samples. A similar approach was used and explained in the details in Espinar et al. [28].

2.3. Lake Breeze Characterization

Unlike natural lakes, human-made reservoirs cause changes in land cover (LCC) that affect the mass, energy, and momentum exchanges between surface and atmosphere, and consequently the regional climate. The contrast between water–land surfaces, regarding the heat capacity, surface albedo, and roughness, lead to a mesoscale circulation non-existing in the region before water impoundment [29]. Segal and Arritt [30] classified a perturbed area (PA) as a contiguous region clearly distinguishable from their surroundings in terms of sensible heat flux (H), which, therefore, can induce a thermal flow similar to the sea breezes. Doran et al. [31] estimated the smallest size (L) of a PA based on the ambient wind speed (u_a) and the average potential temperature (θ) in the atmospheric boundary layer (Equation (4)).

$$L = \frac{\theta}{g\Delta(w'\theta')_s} \frac{u_a^3}{4ln(2)} \tag{4}$$

where g is the gravity acceleration and $\Delta(w'\theta')_s$ is the difference in heat flux between the PA (water reservoir) and the surrounding area.

2.4. Evaluation of Lake Breeze Influence on Incoming Shortwave Radiation

The clearness index was used to evaluate the lake breeze's effect on the incoming solar irradiance at the water surface and the land areas surrounding the Serra da Mesa reservoir. The clearness index is defined by Equation (5),

$$k_t = \frac{GHI}{GHI_0} \tag{5}$$

where GHI and GHI_0 are the incoming global horizontal solar irradiance at the surface and the top of the atmosphere, respectively. The GHI_0 is easily obtained based on the geographical location data and the solar zenith angle.

The relation between clearness index (k_t) and the effective cloud cover (C_{eff}) obtained from satellite imagery was first introduced by Moser and Raschke [21] and constitutes a critical parameter in many radiative transfer numerical algorithms [22,32,33]. The surface incoming solar irradiance depends only on the atmospheric transmittance in cloudless sky condition (τ_{clear}) when $C_{eff} = 0$. On the other hand, in the condition $C_{eff} = 1$, the atmospheric transmittance (τ_{cloud}) corresponds to an overcast sky, with maximum cloud optical thickness and absence of beam solar radiation reaching the surface. The range between these two transmittances defines the slope of the function that converts C_{eff} into global solar horizontal irradiance (GHI) at the surface (Equation (6)).

$$k_t = \frac{GHI}{GHI_0} = \left\{\left(1 - C_{eff}\right)(\tau_{clear} - \tau_{cloud}) + \tau_{cloud}\right\} \tag{6}$$

The τ_{clear} values depend only on atmospheric gases, aerosols, water vapor, and air mass, while the τ_{cloud} values are a function of the maximum cloud optical depth since the cloud transmittance is the major modulating factor of the incoming solar irradiance in the overcast condition. It is reasonable to assume relatively stable values for both τ_{clear} and τ_{cloud} within similar climatic zones. From Equation (6), $k_{t\_clear} = \tau_{clear}$ for cloudless sky condition ($C_{eff} = 0$) and $k_{t\_cloud} = \tau_{cloud}$ in a totally cloudy sky condition ($C_{eff} = 1$).

We selected solar irradiance data for clear skies from three representative measurement sites to estimate typical k_{t_clear} values observed in the Serra da Mesa Reservoir region. The parameters for a simple cloudless sky model, described in Equation (7), were fitted to account for solar zenithal angle (air mass) influence in k_{t_clear} values [34],

$$k_{t\_clear} = k_{0t\_clear}.(cos(\theta_z))^{1.15} \tag{7}$$

where θ_z is the solar zenithal angle and k_{0t_clear} the clear sky transmittance for $\theta_z = 0$.

The inference of the typical k_{t_cloud} value for the Serra da Mesa reservoir region from ground measurements was challenging because the thickest clouds are rare, reducing the confidence of extreme values from k_t distribution. So, we adopted a constant value of $k_{t\_cloud} = 0.05$ based on previous irradiance modeling studies [22,35].

3. Results

3.1. Characterization of Local Climate from In Situ Data

Figure 3a shows the monthly averages of wind speed measured at the buoy measurement site and precipitation measured from 2005 to 2010 at hydrological measurement site managed by ANA (Brazilian Agency for Water Resources).

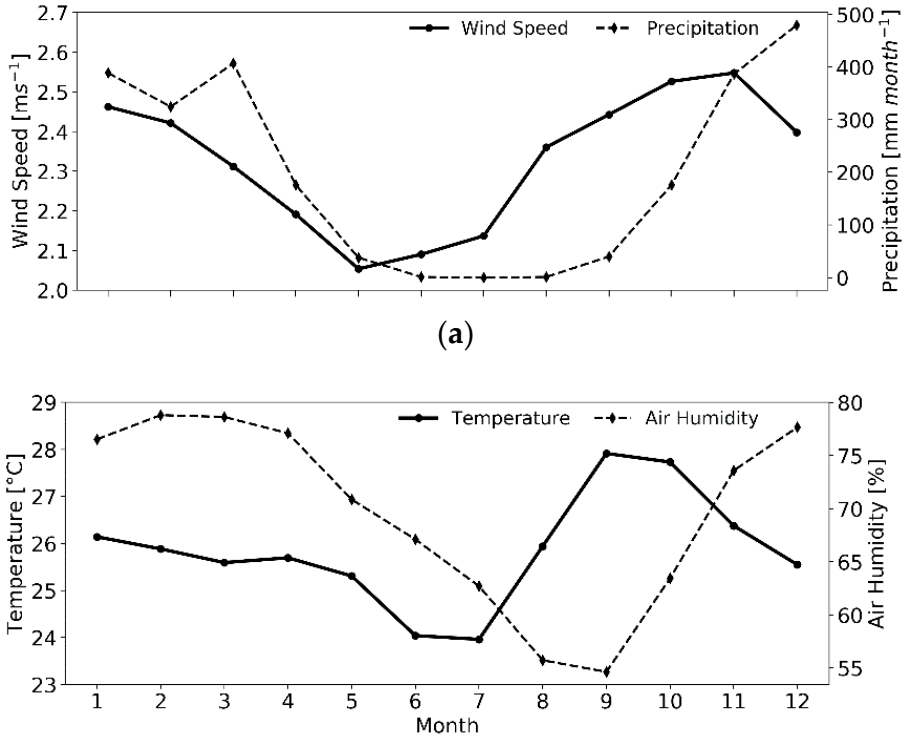

Figure 3. Climate seasonal patterns observed at the Serra da Mesa Reservoir over the period of 2005–2010: monthly mean of (**a**) precipitation (mm month^{-1}) and wind speed (ms^{-1}); (**b**) air temperature (°C) and relative humidity (%).

The precipitation shows a strong seasonal pattern defining a rainy season with precipitation larger than 300 mm per month from November to March. The precipitation is meager from May to September. The average wind speed ranged from 2.4 ms^{-1} to 2.6 ms^{-1} in the rainy season, but it decreased to 2.1 ms^{-1} at the beginning of the dry season (May to July).

The average air temperature in the rainy season ranges from 26 °C to 28 °C and breaks down to 24.5 °C in June–July (Figure 3b). The reduced daily (Figure 4a) and annual (Figure 4b) range of near-surface air temperature, known as an effect of tropical lakes on the regional climate, was previously observed in the Elqui Valley Reservoir for an arid region of Chile [36], for the great African lakes [37], and Lake Sobradinho, a large reservoir in Northeastern Brazil [14].

The relative humidity (RH) has seasonal pattern related to the air temperature, but with a small shift in the minimum RH value (57%) towards August and September. Moreover, during the rainy season, the humidity can reach up to 80% (Figure 3b).

Figure 4 shows the daily and seasonal profiles of air temperature and water temperature over the reservoir. The seasonal pattern of thermal stratification in the Serra da Mesa Reservoir has developed in spring and persisted until summer, with a mean upper amplitude of 5 °C between the surface and bottom in both seasons. During the mixing period (autumn and winter) a nearly homogeneity had been reached (Figure 4c).

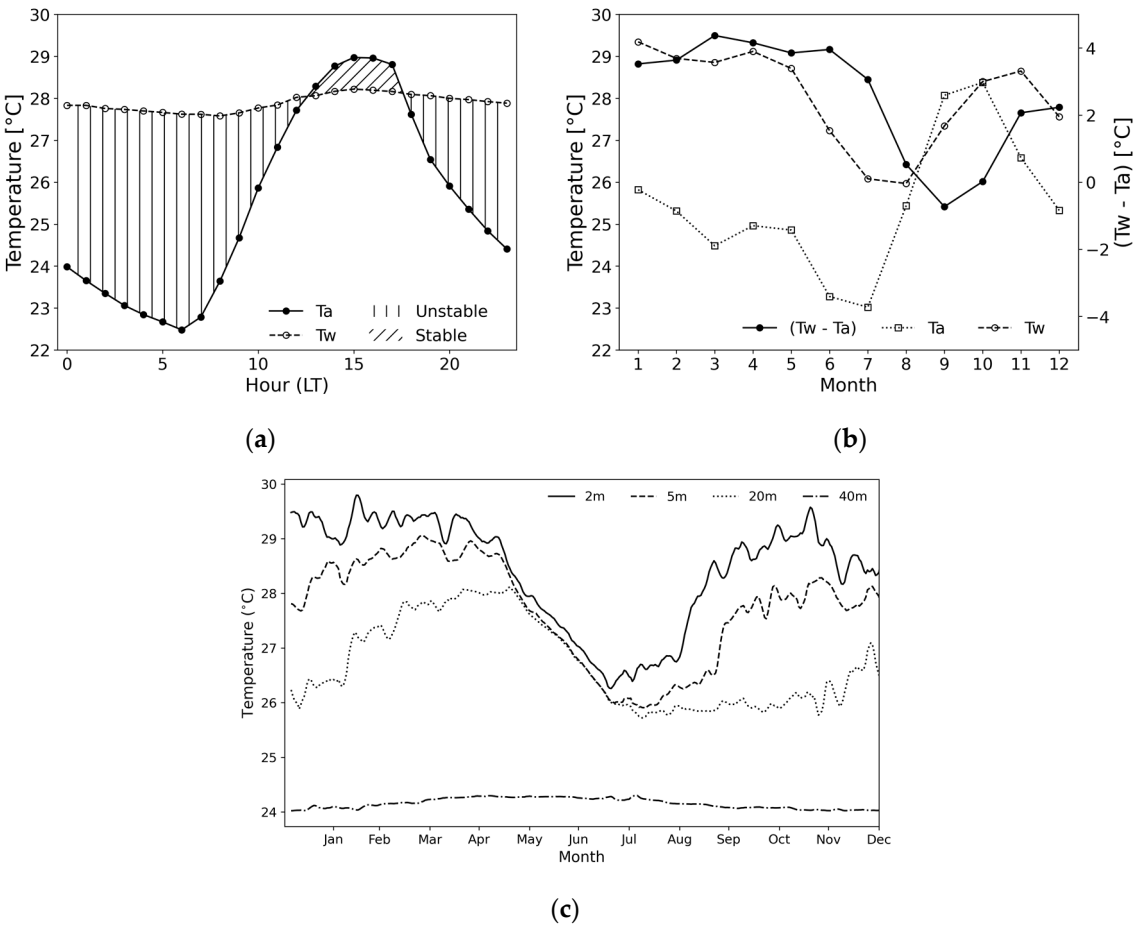

Figure 4. (**a**) Diurnal and (**b**) seasonal cycle for the air temperature (Ta) and water surface temperature (Tw) in Serra da Mesa reservoir. (**c**) Seasonal cycle of water temperature for various depths of the reservoir. Unstable and stable periods shown in the diurnal cycle: (**a**) refers to thermal stratification estimate of the bottom layer (2-m thick) of air over the water surface.

3.2. Identification of Lake Breeze from In Situ Data

The prevailing wind direction (Figure 5a) is from the Northeasterly (≈80°) in the early morning, and changes suddenly to southwesterly (≈250°) after 10 h local time (LT).

Figure 4c,d also shows the lake breeze starting around 10 h LT and wind direction remaining relatively constant from the Southwesterly (from the lake to surroundings) throughout the afternoon but veered to the Northeasterly (from surroundings to the lake) in the midafternoon (17 h LT). In general, the wind speed is low enough to allow a thermally driven secondary circulation to develop over the lake surface (Figure 5b). Such circulation is the lake breeze, as previously documented in the literature [15,29,38].

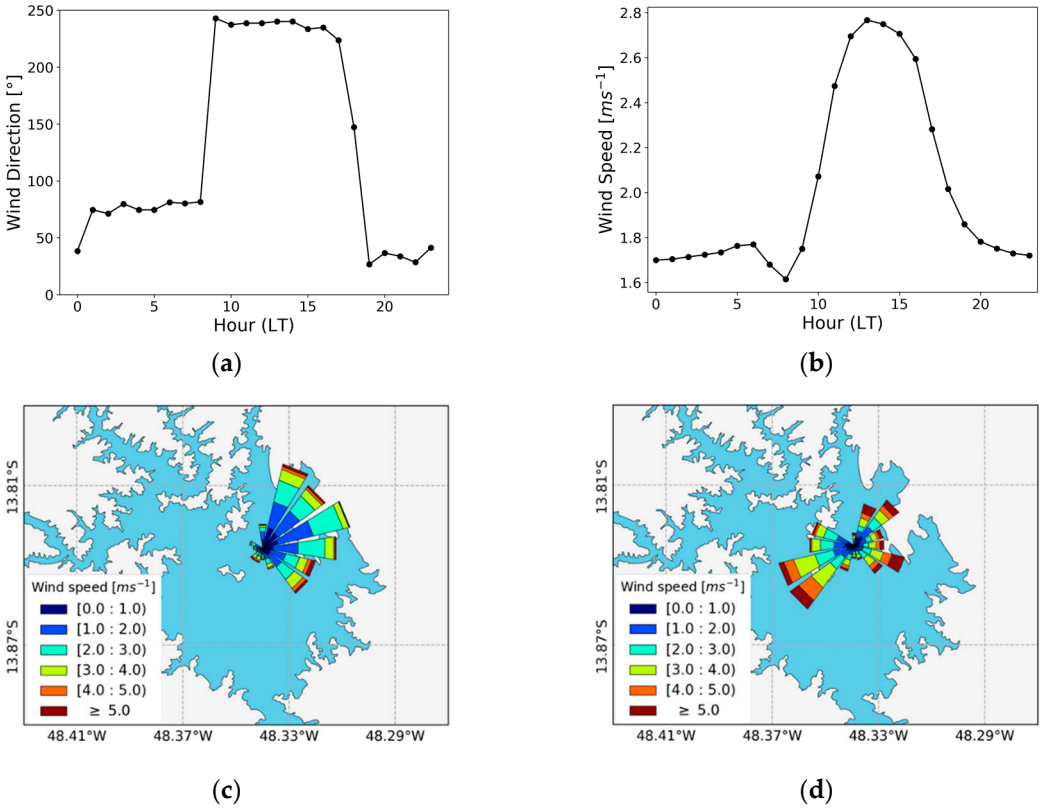

Figure 5. Diurnal cycle of mean hourly wind: (**a**) direction (mode) and (**b**) speed. Wind rose for data acquired (**c**) from 20 h till 09 h LT and (**d**) from 10 h till 17 h LT. Obtained from data acquired in the period from 2005 to 2010.

During the morning hours, the hourly mean wind speeds were 1–2 ms^{-1} and from the north–northeast direction. In the midafternoon, the wind direction shifted to a westerly simultaneously with the increase of wind speed to ~3 ms^{-1}, consistent with the development of a lake breeze circulation. As this feature is commonly observed around the entire perimeter of the inland aquatic system and for weak synoptic wind, it would be associated with a typical low-deformation lake-breeze circulation. This result describes an elementary difference between the dynamics of lake breezes and sea breezes [39]. As found by numerical simulation for gulfs and lakes elsewhere [40], circulations on each shoreline do not occur independently but interact to form a mesoscale high pressure on the surface with associated subsidence over the water. This result has been confirmed by previous studies [5,41,42] and probably defines the most relevant difference between the dynamics of lake breezes and the sea breezes.

According to Equation (4), the required reservoir width (L) to initiate a lake breeze depends on the third power of the wind speed, and it is inversely proportional to the difference in sensible heat flux between the lake surface and its surrounding area. Doran et al. [31] imposed a simple linear decrease of wind speed with distance to derive Equation (4). Figure 6a shows the typical diurnal cycle of the fluxes H observed during the dry season for the Brazilian Cerrado (wooded grassland, savanna) [43] and for a typical Brazilian tropical reservoir [44].

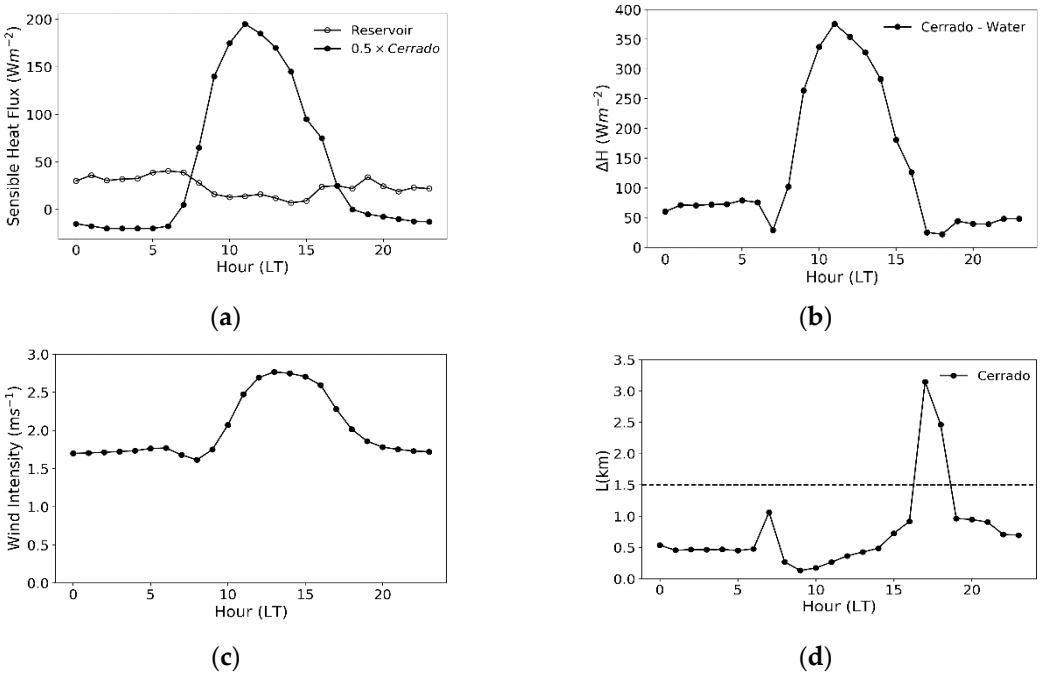

Figure 6. (**a**) Daily variability of sensible fluxes (H) as observed at a typical central Brazilian Cerrado area (solid line, from Miranda et al. [43]) and central Brazilian reservoir (dash-dotted, from Lorenzzetti et al. [44]) during the dry season; (**b**) difference between H in the reservoir and its surroundings (solid line—cerrado); (**c**) diurnal variability of ambient wind speed, and (**d**) minimum reservoir width, L, necessary to create a closed circulation. The horizontal line in panel (**d**) indicates the typical width of the Serra da Mesa reservoir.

The sensible heat flux averaged to 330 W/m^{-2} in the Cerrado area and only 25 W/m^{-2} over the reservoir (Figure 6a). As can be noticed, the sensible heat flux over the water remained low throughout the day (from 10 to 40 W/m^{-2}), while the maximum flux over the Cerrado exceeded 300 W/m^{-2}.

The difference between the heat fluxes over land relative to the water surface is presented in Figure 6b, while Figure 6c shows the daily cycle of the ambient wind speed (u_a) at 10 m height. For the assessment of u_a (Equation (4)), in order to differentiate the reservoir-modified wind, we considered the ambient wind speed as measured by the ridge-top site (A24 in Figure 1 and Table 2) (for details see Appendix A). The hourly values of both variables were used in Equation (4) to estimate the minimum lake width (L) required to initiate a closed atmospheric circulation. The horizontal line in Figure 6d represents the typical width of the Serra da Mesa Reservoir. There are conditions for lake breeze occurrence whenever the estimated values for L are below the horizontal line. The required lake width is larger than the typical width of the Serra da Mesa Reservoir only between 17 h and 19 h LT (Local Time).

The strength of the synoptic wind, together with its direction relative to the shoreline, also has a prevailing influence on the inland penetration of the lake breeze [42,45–48], though other factors such as orography, lake–land temperature gradient, and even soil moisture can be distinguished [49]. These factors, added to the fact of wind speed that was low enough (Figure 6c), allowed a thermally driven secondary circulation to begin to develop over the Serra da Mesa Reservoir. A weak to moderate onshore synoptic wind favors the formation of surface divergence areas over the water, while increasing wind will displace it downwind and finally inhibit breeze formation [39].

3.3. Spatial Analysis of Cloudiness on the Reservoir Area

Maps of C_{eff} were obtained from GOES-16 visible imagery based on Equation (1) with a 1-h time step for a region covering up to 100 km far from reservoir shores (hereinafter referred to as the

domain region). Figure 7 shows the seasonally averaged cloud patterns over the water surface and the surrounding areas for morning and afternoon periods.

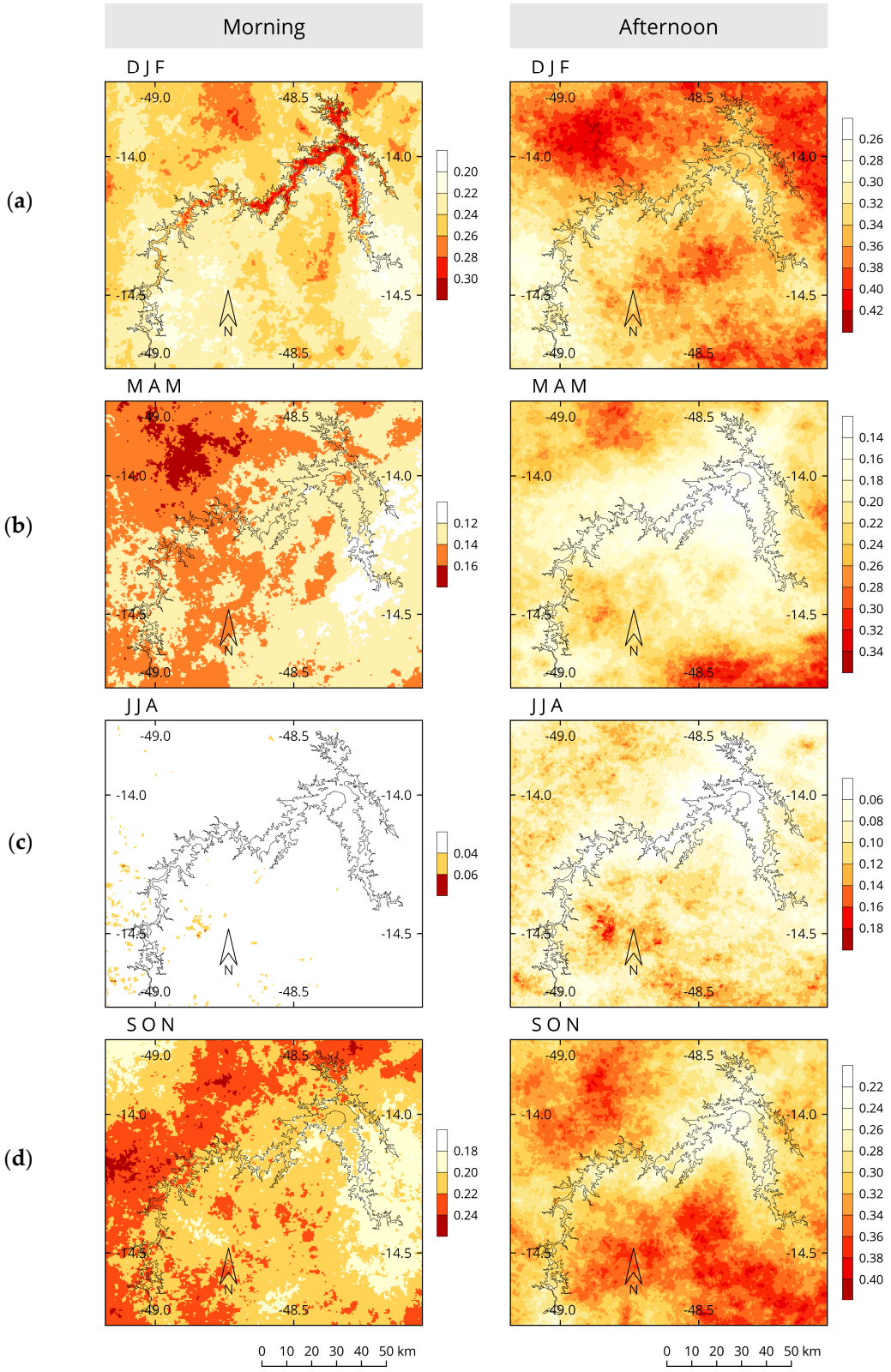

Figure 7. Seasonal maps of average C_{eff} estimates (%) over the Serra da Mesa Reservoir for the morning (9–11 h LT) and afternoon (14–16 h LT) periods for (**a**) December, January, February (DJF); (**b**) March, April, May (MAM); (**c**) June, July, August (JJA); and (**d**) September, October, November (SON).

Morning maps comprise images acquired from 09 h to 11 h LT, while afternoon maps comprise images from 14 h to 16 h LT. All maps retain the same 500 m horizontal resolution of the original satellite imagery. There is a negligible difference between cloudiness over the lake and surroundings (external) areas far from the lake borders during the morning period, apart from increased cloudiness over the lake during austral summer (DJF). This anomaly was caused by sun glint phenomenon, observed in visible satellite images acquired from January 1st to 26th and from December 5th to 31st of 2018, steadily at 10 h LT, therefore it is not related to cloudiness (for details on sun glint detection see Appendix B). No evidence of sun glint was detected for other periods, and geometrically it would be unlikely, although this possibility cannot be ruled out completely.

Compared to the surrounding dry land, the lower cloudiness over the lake is noticeable during the afternoons in the maps. The C_{eff} over the lake surface is ~0.04 (~12%) lower than over dry land during summer (DJF), and up to 0.08 (~30%) along with the fall season (MAM) and spring (SON). Nevertheless, some level of uncertainty in these values remains due to interannual variability. Remarkably, the maps show a slight southwestward drift in the cloudless signature due to prevailing Northeasterly winds in the region.

The visual observation indicated the need for statistical analysis to evaluate the lake breeze's influence on cloud cover. Thus, we took six target areas at different locations inside the domain region: the water surface, defined as the contiguous flooded area presenting at least 2 km width; the borders, outlined as the 2 km buffer from the shores; and four external (surrounding dry land) areas, distributed at cardinal regions (N, E, S, W) more than 2 km far from the reservoir shores as shown in Figure 8. These four external areas were chosen in locations presenting similar topography of the original (pre-flooded) reservoir area.

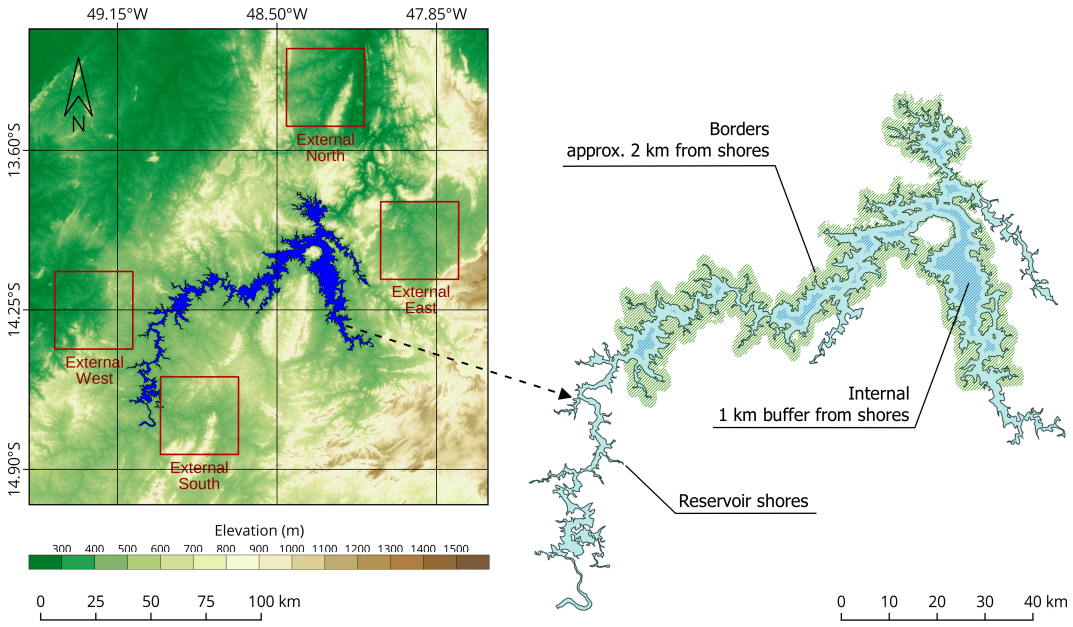

Figure 8. The topography of the region around Serra da Mesa reservoir and location of the six target areas used for cloudiness comparisons. Four external areas (**left**), the borders, and internal areas (**right**).

To acquire the representative hourly cloudiness observed by satellite in each target area, we calculated the average of hourly C_{eff} values for 50 pixels (0.25 km^2) randomly sampled in each of the six target areas (internal, borders, and external—N, E, S, W). Finally, the cloudiness in external samples was evaluated in two ways: (a) the four external areas were analyzed independently, and (b) the four external data were appended together to form one general external area, retaining the cloudiness variance observed in each target area.

Figure 9 shows the daily cycle of hourly average cloudiness for 2018.

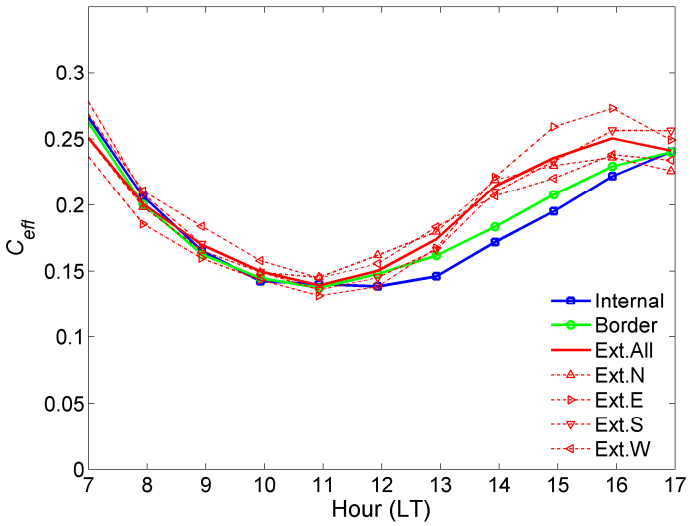

Figure 9. Hourly averaged cloudiness C_{eff} for the target areas at Serra da Mesa reservoir during the year of 2018.

The line graph endorses the lake breeze's recurrent characteristics, starting around 12 h LT and producing differences in C_{eff} values of up to 0.05 (25%) between the internal and external areas of the reservoir. The borders show an intermediate pattern, but closer to internal (water surface) than external area. Table 3 lists the detailed information, including the relative gain in cloudiness relative to the water surface. The results validate the findings from the visual observation C_{eff} from Figure 7. The cloudiness increases as we move away from the reservoir in any of the four cardinal directions. The same pattern is observed when looking at the afternoon-only cloudiness (14 h to 16 h LT). Comparing the cloudiness over the water surface area to the cloudiness over the combined external areas, one can notice a decrease of 5.7% and 19.0% in the average C_{eff} for daily and afternoon periods, respectively.

Table 3. Comparison of C_{eff} averages for daily (7–17 h LT) and afternoon (14–16 h LT) timeframes for all target areas of the Serra da Mesa Reservoir.

Target Areas	Daily (7–17 h)	Relative Difference to the Internal	Afternoon (14–16 h)	Relative Difference to the Internal
Internal	0.187	-	0.196	-
Border	0.188	0.5%	0.207	5.4%
External North	0.196	4.7%	0.229	16.4%
External East	0.197	5.0%	0.251	27.9%
External South	0.200	6.6%	0.233	18.7%
External West	0.199	6.4%	0.222	13.0%
External Combined	0.198	5.7%	0.234	19.0%

Figure 10 depicts the empirical cumulative distribution function (CDF) of C_{eff} values in both morning and afternoon periods. Figure 10a shows similar cumulative cloudiness frequencies in all target areas during the morning (09 h to 11 h LT). Figure 10b shows a detached pattern for the water area during the afternoon (14 h to 16 h LT), as expected from previous results. The conclusions are twofold: first, the reduced daily average cloudiness over the water surface is a consequence of the cloudless afternoons engendered by the lake breeze, and second, the lake breeze induced a local cloudiness anomaly, as all of the four external areas presented increased cloudiness, which would be very unlikely to occur by chance.

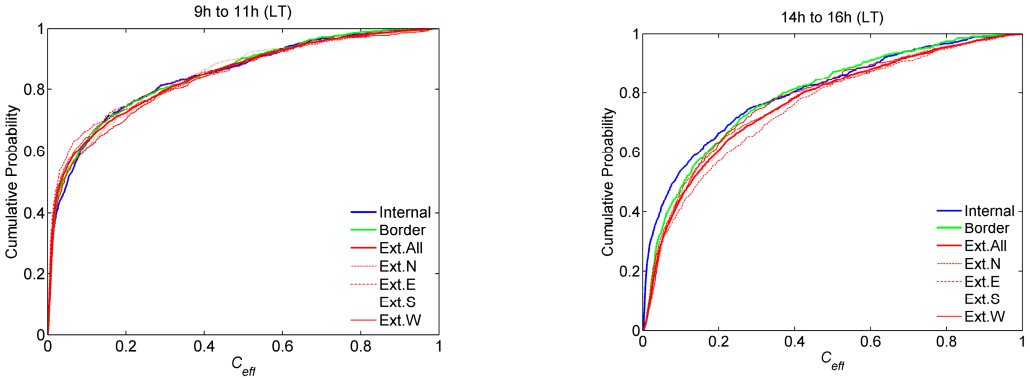

Figure 10. The cumulative distribution functions (CDF) charts for effective cloud cover C_{eff} levels for each target area during the (**a**) morning and (**b**) afternoon periods.

Table 4 summarizes the K–S test results comparing the cloudiness CDFs over the water surface area and dry land areas. The alternative hypothesis ($H1$) implies that the cloudiness CDF over external areas is lower than the CDF over the water surface, indicating that the cloudiness in the external area tends to be larger than the internal area. The p-values presented are the Type 1 error, understood as the probability of rejecting the null hypothesis considering it is true. Daily and afternoon p-values are extremely low, indicating high confidence that the distributions are different (alternative hypothesis $H1$ is true). On the other hand, there is a higher p-value of 1.81×10^{-2} for the morning, indicating increased uncertainty in assuming the null hypothesis is false.

Table 4. p-values for Kolmogorov–Smirnov (K–S) one-sided test comparing the empirical cumulative distribution functions of effective cloud cover (C_{eff}) in the wet (internal) and dry (external) areas of the reservoir. Null hypothesis, $H0: \mu_{Internal} = \mu_{External}$, where μ denotes the mean value of the distribution from which samples were drawn.

Alternative $H1$	p-Value Daily	p-Value Morning	p-Value Afternoon
$\mu_{Internal} < \mu_{External}$	1.30×10^{-16}	1.81×10^{-2}	6.52×10^{-20}

Figure 11 shows absolute differences of cumulative cloudiness probability for internal area ($CDF_{internal}$) and external area ($CDF_{external}$) along C_{eff} values for daily, morning only, and afternoon only periods. The corresponding critical bounds, V_c, for a 99% confidence level are plotted over.

The plot shows CDF differences exceeding the critical bound for C_{eff} up to 0.20 for daily averages, and up to 0.40 for afternoon averages. It indicates a higher frequency of lower Ceff values in the internal area when compared to the external area. This result supports the hypothesis that the reservoir affects mostly shallow convection since deep convective clouds are both brighter ($C_{eff} >> 0.4$) and less susceptible to surface influence at the local scale. The K–S test results bring more evidence that cloudless skies frequency over the water surface is higher than outside the Serra da Mesa Reservoir.

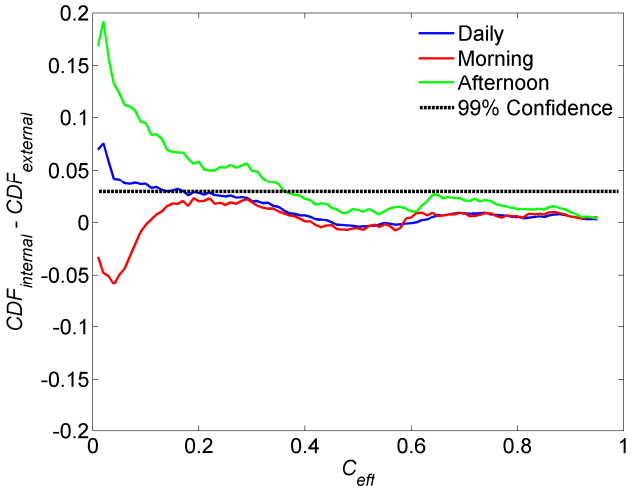

Figure 11. Absolute differences of cumulative cloudiness probability for internal area ($CDF_{internal}$) and external area ($CDF_{external}$) along C_{eff} values for Serra da Mesa hydropower plant. The horizontal line represents the one-sided test bound V_c at a 99% confidence level.

3.4. Time Analysis of Cloudiness over the Reservoir

So far, our results have shown that a spatial cloudiness pattern exists and that the reservoir probably induces it. Nevertheless, one could still argue that the internal and external areas of the reservoir are not similar enough and that other factors than the reservoir itself could impact the local cloudiness. Figure 12 presents a proxy to overcome this issue.

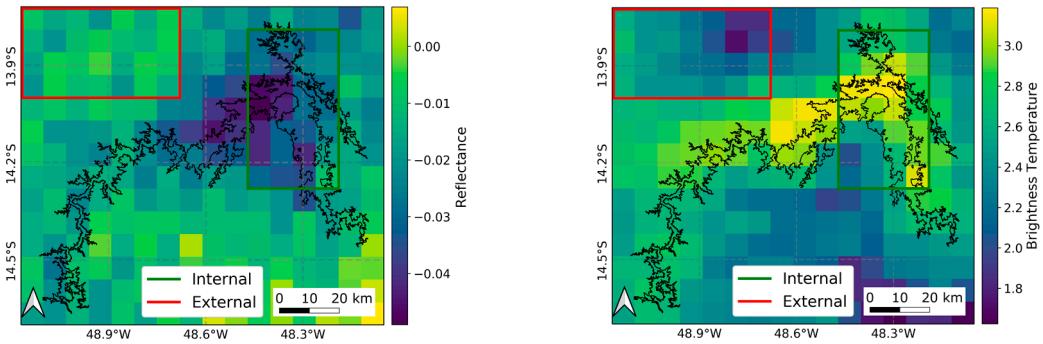

(**a**) (**b**)

Figure 12. Mean differences (after–before) between periods after (1997–2009) and before (1984–1996) of the reservoir construction over Serra da Mesa Basin for (**a**) visible reflectance (0.6 µm) for 15 h LT and (**b**) daily infrared brightness temperature (11.0 µm) in K. Green and red rectangles show domains for internal and external cloudiness evaluation.

The long-term mean differences of temperature and reflectance after and before the reservoir construction is presented in Figure 11, respectively. The comparison analysis used local cloudiness data estimated from the GridSat-B1/ISCCP dataset in two distinct time frames, as described earlier in Section 2.2.

As a first approximation, both images suggest that the cloudiness over the external areas exceeds cloudiness over the water surface of the reservoir. Therefore, Figure 12 endorses our and other recent results [5], pointing out that the presence of the reservoir induces a lake breeze system that inhibits the cloud formation because of dry air subsidence from the upper atmospheric layers to near-surface levels above the water surface. However, Evan et al. [50] suggest that the difference in cloudiness

frequency may be due to satellite viewing geometries affecting the cloudiness data acquisition on a long-term basis.

If the changes in the reflectance (R) (Figure 12a) and in the infrared brightness temperature (BT) (Figure 12b) were associated with satellite viewing geometry artifacts, it would affect the overall sampled area in a similar way. Both images in Figure 12 show that it is not the case, as the cloudiness reduction over the widest area of the water surface of the reservoir exceeds cloudiness reduction over the external areas. The differences in the external area present smaller magnitudes and may be attributed to surface heterogeneity and limitations in the sampling process due to interannual variability.

Figure 13a,b shows the histograms of the mean visible reflectance data over the water surface area in the same timeframes used earlier "before" and "after" the flooding of the hydropower reservoir.

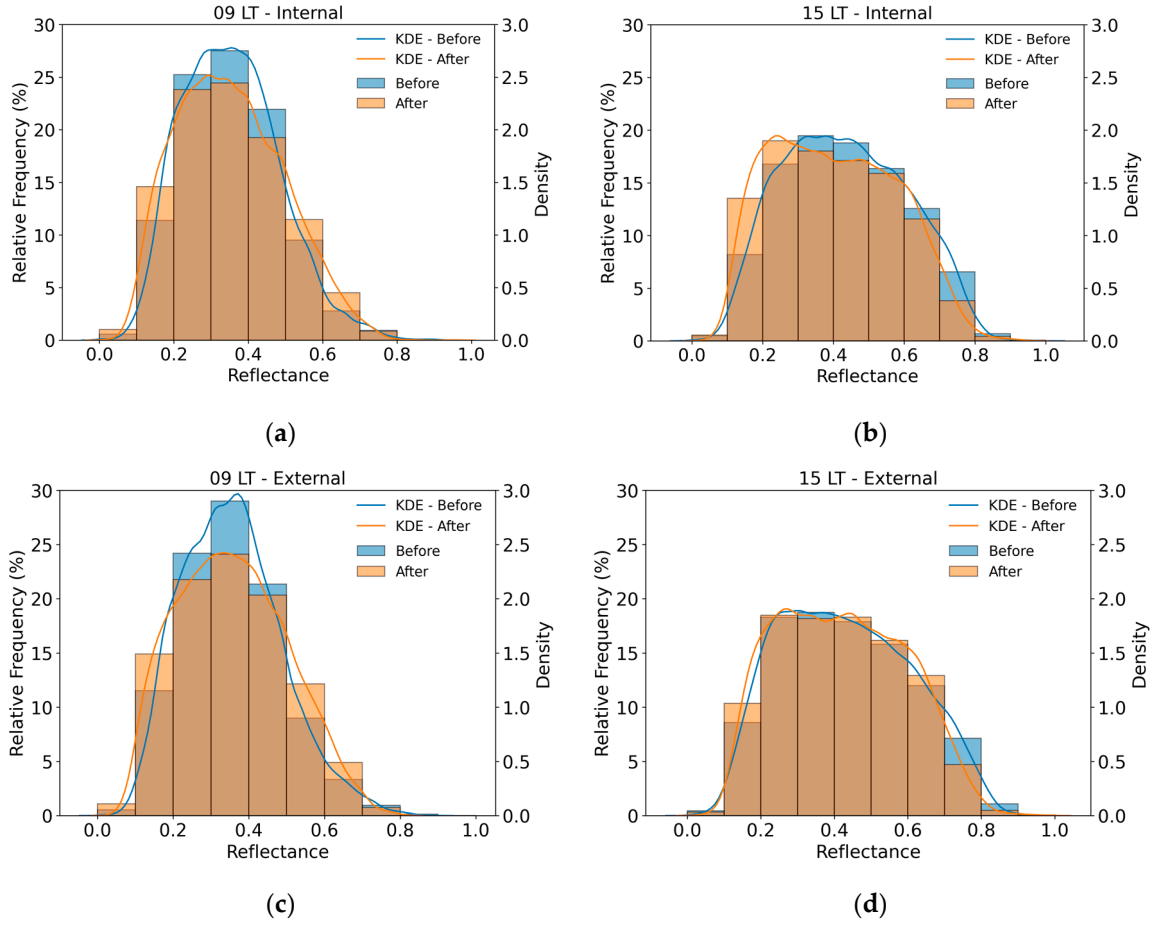

Figure 13. Relative frequency histogram (%) and kernel density estimates (KDE), right axis, of visible reflectance (R) over the water surface area based on GridSat-B1/ISCCPP data acquired before (blue boxes) and after (brown boxes) filling the Serra da Mesa Reservoir: (**a**) 09 h LT (morning period) in the internal area; (**b**) 15 h LT (afternoon period) in the internal area; (**c**) 09 h LT (morning period) in the external area, and (**d**) 15 h LT (afternoon period) in the external area.

In the same way, Figure 13c,d shows histograms of cloudiness frequency over the reservoir's external areas.

Figure 12a,c shows the histograms obtained for 9 h LT in both timeframes (after and before the flooding). Both present very similar profiles with the maximum frequency occurring in quite the same visible reflectance. Nevertheless, the histograms obtained for 1997–2009 (the after flooding period) presents more spread than the one obtained for 1984–1996 (before filling). The histograms for the afternoon period (15h LT), shown in Figures 13b and 12d, also have very similar profiles, except for a left shift on the maximum frequency after filling the reservoir. Considering the typical reflectance

values for surface (0.08 to 0 0.15) and cloud top (0.5 to 0.9), this shift suggests that the reduction in visible reflectance is linked to a decrease in the cloudiness frequency. In the afternoon, no discernible change of cloudiness frequency occurs in the visible reflectance for the external areas surrounding the reservoir. The K–S test results endorse this conclusion comparing the empirical frequency distributions of reflectance raw data (Table 5). The null hypothesis at a 1% significance level is rejected only for the distributions observed in the water surface area during the afternoon (p-value = 3.74×10^{-3}). Such results point out that the statistically significant change in cloudiness induced by the hydropower lake occurred only over the water surface area during the afternoon. Moreover, the influence of the satellite viewing geometry was discarded once the shift occurs only for part of the Serra da Mesa hydropower area.

Table 5. p-values for K–S two-sided hypothesis test comparing the empirical frequency distribution of cloud reflectance (R) raw data in the internal and surroundings (external) areas of the reservoir. Null hypothesis $H0: \mu_{after} = \mu_{before}$.

Alternative Hypothesis $H1$	p-Value Morning (9 h LT)	p-Value Afternoon (15 h LT)
Internal : $\mu_{after} \neq \mu_{before}$	5.03×10^{-1}	3.74×10^{-3}
External : $\mu_{after} \neq \mu_{before}$	8.94×10^{-1}	4.16×10^{-1}

Figure 14a,b shows the boxplot of the monthly mean of reflectance observed in the internal and external areas at 15 h LT throughout the year for the same two timeframes 1984–1996 (before filling the reservoir) and 1997–2009 (after filling the reservoir). Figure 14a demonstrates that the most substantial differences in the median of the observed reflectance occur during the winter season from July to September. Decreased reflectance values were observed after reservoir filling. The mismatched notches indicate that these samples are significantly different. This long-term observation confirms the GOES-16 previous results and suggests a reduced cloudiness area over the water. However, it is important to note that June presented an increased reflectance after reservoir filling, differently from other months. The existence of fewer data samples (553 samples before and 395 samples after) may have affected uncertainty, widening the notches. In this sense, the overlapped notches for June indicate that the datasets are not significantly different at a 95% confidence level, leading to a non-conclusive comparison.

Another possible cause for this distinct result relies on the fact that in June, the reservoir surface temperature exceeds surface air temperature and tends to produce an unstable atmospheric boundary layer (ABL), as anticipated by Garrat [51]. Water surface temperatures (T_w) are, on average, higher than air temperatures (T_a) (Figure 3a,b). The ABL over the Serra da Mesa Reservoir remains unstable ($T_w > T_a$) around 3/4 of the time on a monthly scale (Figure 4b). However, the stability of the ABL varied at both diurnal (Figure 4a) and seasonal timescales (Figure 4b). Unstable ABL conditions were prevalent in summer and autumn, but June is the month marked by the higher gradients between the reservoir surface and atmosphere (Figure 4b). The maximum decrease for the water column temperature until 20 m depth occurred for June (Figure 4c), resulting in a consistent and persistent gradient between the reservoir surface and atmosphere. The mean values of T_w and T_a presented in Figure 4 are based on 3-year data acquired in the Serra da Mesa reservoir. More investigation is required to clarify the reason for this behavior in June. Nevertheless, it happened consistently during the data acquisition period. The lower wind speeds for June (Figure 3a) resulted in less mechanical mixing at the lower ABL and, consequently, an enhanced unstable ABL. Possibly, the cloudiness may be increased due to enhanced evaporation from the water surface after reservoir flooding. Meanwhile, Figure 14b shows slighter differences in reflectances between the two periods most of the year for the external area.

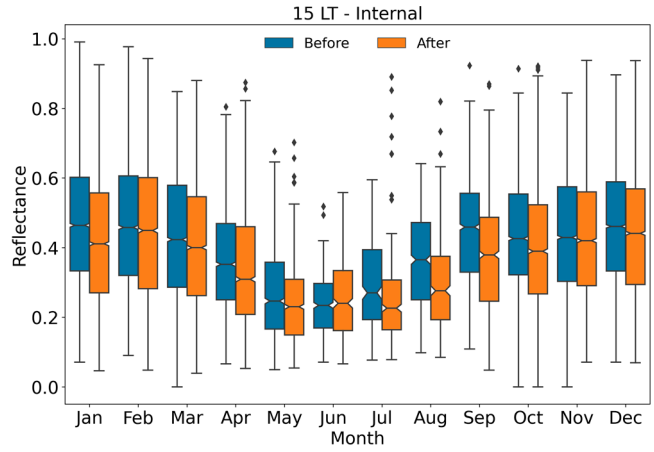

(**a**)

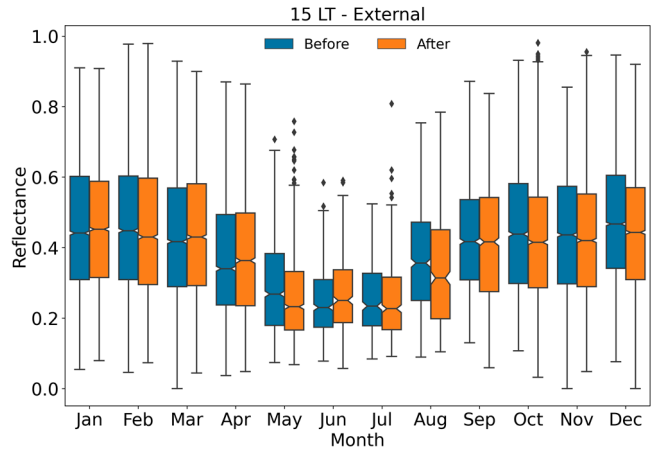

(**b**)

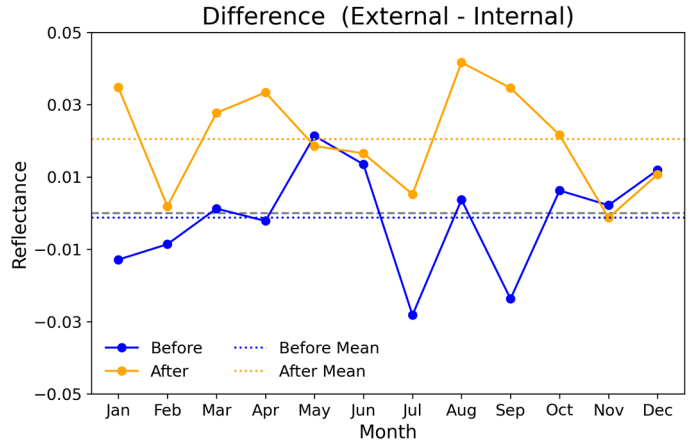

(**c**)

Figure 14. Boxplot for the monthly visible reflectance observed in the internal (**a**) and external (**b**) reservoir area at 15h LT before (blue boxes) and after (orange boxes) construction of the Serra da Mesa hydropower plant. Panel (**c**) shows the difference between external and internal areas for the period before and after lake filling. The box represents the interquartile range (IQR) (25–75%), and the whiskers are the +/− 1.5 × IQR bounds of data values. The notch (horizontal line) indicates the median (95% confidence). Overlapped notches mean the datasets are not significantly different at 95% confidence level [52].

An irregular behavior is noted in the dry months (May to August) possibly affected by fewer data samples as mentioned before. A small reduction is also noted at the end of the year (October to December). This result reveals the uncertainty inherent to the sampling method. Factors such as interannual variability and land cover change may affect cloudiness unevenly along the years, so that identical distributions for the periods before and after reservoir filling are unlikely to occur at monthly scales. To overcome partly of this limitation, Figure 14c shows the relative difference between the reflectance from external and internal areas for each period mentioned above. The reflectance differences oscillate near zero (mean = −0.0013) before reservoir filling, while the differences oscillate around positive values (mean = 0.0204) after reservoir filling. This result supports previous findings that suggest the existence of a considerable impact on cloudiness frequency caused by the Serra da Mesa Reservoir.

3.5. The Lake Breeze Influence on Surface Incoming Solar Irradiation

An estimate of the typical k_{0t_clear} value for the Serra da Mesa reservoir was obtained by fitting Equation (7) to the global solar irradiance data acquired in three ground measurement stations near the hydropower dam. Cloudy samples were manually screened and data were converted to observed clearness index (k_{t_clear}). The fitting procedure was performed for 5-degree intervals of the solar zenith angle in order to reduce uncertainties in k_{0t_clear} estimates. Ground data acquired at a solar elevation lower than 20° were discarded.

Table 6 summarizes the results for k_{t_clear} values obtained in each ground measurement site for two solar zenith angle intervals. The last line shows the results obtained by fitting the model for data from the three sites altogether. The k_{t_clear} listed in the last line was assumed as the regional values. The difference between the regional k_{t_clear} and the site-specific k_{t_clear} ranges from 1.3% for low zenith angles to ~3.5% for high zenith angles.

Table 6. List of ground measurement sites near the Serra da Mesa Reservoir used to estimate the cloudless atmospheric transmittances k_{t_clear} values. The simple model, described in Equation (7), provided the k_{t_clear} values for 5-degree intervals of solar zenith angles. The table presents the results for two of the intervals. The last line exhibits the results obtained by using data from the three measurement sites altogether to estimate regional k_{t_clear} values.

Met. Station	k_{t_Clear} **($\theta z < 5°$)**	k_{t_Clear} **($55° < \theta z < 60°$)**
BRB	0.760	0.710
A22	0.750	0.670
A24	0.770	0.680
Regional k_{t_clear}	**0.759**	**0.685**

The clearness index k_t was calculated using Equation (6) for C_{eff} values provided by GOES-16 as a function of day and time and then averaged over the year for three areas: internal (water surface), reservoir borders, and external areas. The calculation of GHI was performed by multiplying hourly clearness index (k_t) by the irradiance at the top of the atmosphere according to Equation (5). Table 7 provides information on the enhanced incoming solar irradiance at the water surface of the Serra da Mesa Reservoir compared to the surrounding external areas as reference. Table results demonstrate that reduced local cloudiness increases the annual average of incoming solar irradiance around 1.73% from 7 h to 17 h LT. The solar irradiance enhancement reaches up to 4.51% for the afternoon (from 14 h to 16 h LT).

Table 7. Comparison of annual mean effective cloud cover index, C_{eff}, and respective estimates of mean surface incoming solar irradiance (GHI_{est}) at the water surface and external areas of the Serra da Mesa Hydropower Reservoir. The incoming global solar irradiance in external areas was the reference value to calculate the irradiance enhancement. Morning differences were not significant (not shown).

Region	Daily (7–17 h)			Afternoon (14–16 h)		
	C_{eff} avg.	GHI_{est} avg.	GHI_{est} enhanc.	C_{eff} avg.	GHI_{est} avg.	GHI_{est} enhanc.
Internal	0.187	523.8	1.73%	0.196	549.0	4.51%
Border	0.188	521.6	1.30%	0.207	542.1	3.20%
External Combined	0.198	514.9	-	0.234	525.3	-

4. Conclusions

This work evaluated the formation of the lake breeze in the Serra da Mesa Reservoir, located in the Central region of Brazil, and its impacts on the regional cloudiness climate. The study evaluated the spatial and time distributions of cloudiness based on in situ measurements and two satellite-derived datasets.

In situ data covering a 5-year period taken from an offshore buoy system confirmed a prevailing breeze mechanism in the reservoir that superimposes large-scale atmospheric flow and generates a modified regional wind climatology. The difference between the typical heat fluxes in the internal (water surface) and external areas combined with locally calm winds explains the development of the lake breeze most of the day.

High-resolution satellite imagery was used for assessment and seasonal analysis of the spatial distribution of cloudiness, which identified the lake contour signature on afternoon cloud fields all year long, suggesting a persistent pattern of lake breeze. Moreover, the spatial analysis allowed identifying a statistically significant reduction of ~5.7% in the effective cloud cover index (C_{eff}) over the water surface area compared to the surrounding areas of the reservoir. A more detailed hourly basis analysis showed that the largest cloudiness differences occur from 12 h to 16 h (Local Time).

In addition, two sets of 15 years of satellite images, one before and the other after the reservoir filling, allowed the assessment of the gross impact of the hydropower plant construction on the regional cloud regime. A change in cloudiness frequency distribution was detected after lake filling. Such a difference in cloudiness frequency between before and after was statistically significant, evidencing reservoir impact on regional cloud regime over the flooded area. On the other hand, the external areas surrounding the formed lake did not reveal a significant change in the cloudiness pattern, dismissing any data trend.

In summary, the study strongly suggests that induced lake breeze circulation enhances cloudless skies over the flooded area during daytime at Serra da Mesa. This conclusion was supported by remote and in situ measurements, but some limitations should be mentioned: This is a study case for a specific reservoir and, despite their potential for extrapolation, these conclusions should not be assumed for other tropical reservoirs. Further assessments are needed to evaluate the extent of the phenomenon for other locations. Another limitation concerns the quantitative analysis presented herein. Uncertainty related to the cloudiness sampling method and interannual variability may affect the comparisons, requiring a longer-term analysis to provide climatologically consistent measures.

Furthermore, a preliminary assessment of the incoming solar irradiance at the lake surface indicated an increment of 1.73% on the daily average and up to 4.51% increase for the afternoon timeframe. These are substantial values from the perspective of solar energy resource assessment. The enhancement in horizontal surface solar irradiance over the hydroelectric lake compared to the surrounding areas corresponds to a relative increment in the annual photovoltaic yield from the reported average ranging from 1622 kWh/KWp [53] up to 1696 kWh/kWp. Furthermore, as floating photovoltaic (FPV) plants typically perform better at lower temperatures, an additional gain ranging

from 10% to 15% can be expected according to Rosa-Clot and Tina [54], leading to a net photovoltaic yield for the water surface of up to 1949 kWh/Kwp. Our research team is already working on the next step, i.e., evaluating the solar irradiance enhancement and FPV yield in several hydropower plants operating in different climate regions of the Brazilian territory to provide a solar energy assessment that supports the FPV technology deployment. In the near future, solar-hydro hybrid plants can become a great alternative to integrate both energy resources due to the breeze mechanism in several tropical hydropower dams combined with the high solar irradiance in the Brazilian territory.

Author Contributions: Conceptualization, A.R.G., A.T.A., F.R.M., R.S.C., M.S.G.C. and E.B.P.; methodology, R.S.C., M.S.G.C., E.V.M. and S.V.P.; software, S.V.P. and R.B.P.; formal analysis, A.R.G., A.T.A., M.P.P., F.J.L.L. and R.B.P.; investigation, A.R.G., A.T.A. and E.V.M; resources, M.P.P. and F.J.L.L.; data curation, M.P.P., F.J.L.L. and R.B.P.; writing—original draft preparation, E.B.P., A.R.G., F.R.M. and A.T.A.; writing—review and editing, all authors; visualization, S.V.P. and R.B.P.; supervision, F.R.M.; project administration, E.B.P.; funding acquisition, E.B.P. All authors have read and agreed to the published version of the manuscript.

Funding: This research is a cooperative action funded by the National Institute of Science and Technology for Climate Change—INCT-MC Project Phase 2 (Grants FAPESP 2014/50848-9, CNPq 465501/2014-1, and CAPES/FAPS No 16/2014), Petrobras through ANEEL R&D projects PD-00553-0034/2016 and PD-00553-0042/2016, and FAPESP post-doctoral fellowship (Process 2019/05361-8). CNPq also granted research fellowships for Fernando Ramos Martins, Arcilan Trevenzoli Assireu, and Enio Bueno Pereira.

Acknowledgments: The authors thank NOAA for providing GOES-16 satellite imagery and hosting the International Satellite Cloud Climatology Project (ISCCP) website (https://www.ncdc.noaa.gov/isccp) maintained by the ISCCP research group which provided GridSat B1 product. Thanks also to National Meteorology Institute (INMET) and to SONDA project for providing quality surface data. Finally, we acknowledge the National Institute for Space Research (INPE) for supporting the research team and the essential contribution of the Earth System Science Postgraduate Program (PG-CST) to this research.

Conflicts of Interest: The authors declare no conflict of interest. The funders had no role in the design of the study; in the collection, analyses, or interpretation of data; in the writing of the manuscript; or in the decision to publish the results.

Appendix A

The assessment of lake breeze occurrence according to Equation (4) requires an estimate of ambient wind speed (u_a), defined as the component unaffected by lake breeze. In order to differentiate the reservoir-modified wind, we considered the ambient wind speed as measured by the ridge-top site (A24 in Figure 1).

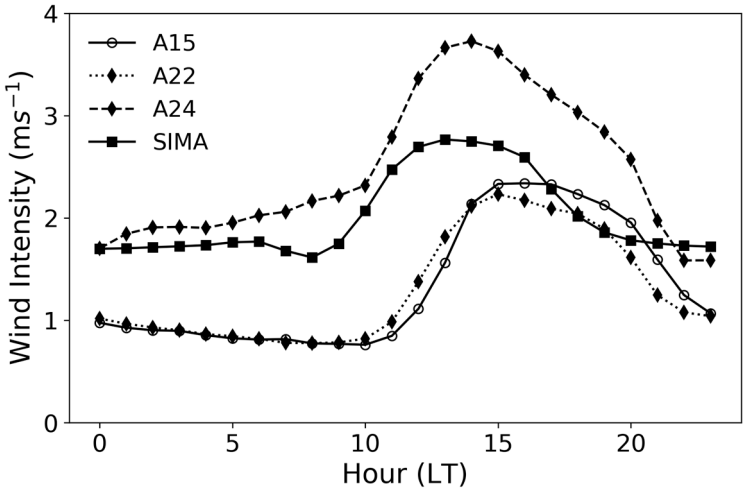

Figure A1. Daily cycle of mean hourly wind speed at three sites nearby reservoir (A15, A22, and A24) and inside the reservoir (SIMA) calculated over the whole period shown in Table 2.

Figure A1 shows the mean daily cycle of wind speed at four sites: SIMA (inside the reservoir), A15, A22, and A24 (surroundings the reservoir). All the sites show a diurnal cycle with a maximum

in the early afternoon. The main aim was to examine how wind intensity on reservoir valley and surroundings (SIMA, A15 e A22) compared with the prevailing wind direction as measured by the ridge-top site (A24) (Figure 1 and Table 2). Figure A1shows that the ambient winds (A24) are more intense than the wind-terrain system (SIMA, A15 e A22), as expected.

Appendix B

The sun glint phenomenon affects satellite visible reflectance measurements due to sunlight specular reflection over water surfaces. It is geometrically dependent and thus presents a recurrent characteristic for geostationary satellites lasting several days at specific hours due to slow change on Earth axis declination. The abnormally high reflectance observed over the water in the austral summer maps shown in Figure 14 caught attention on the possible occurrence of sun glint over the Serra da Mesa reservoir. For its detection, a comparative analysis of surface reflectance for consecutive hours was performed, as shown in Figure A2. The detached pattern of the 10 h LT curve is observed from 5 December to 29 January. The differences from cloudiness prior (9 h) and after (11 h) suggest that clouds did not cause the brightness observed at 10 h.

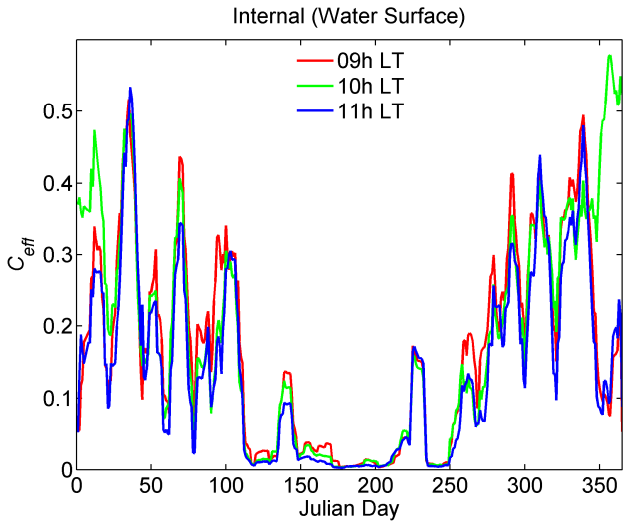

Figure A2. Annual cycle of hourly effective cloudiness index (C_{eff}) for 9 h, 10 h and 11 h LT for the Serra da Mesa reservoir internal area.

Despite the empirical evidence, an analytical evaluation of sun–satellite geometry was also performed to confirm the sun glint occurrence. It is known from basic optics that specular reflection implies identical incidence and reflected zenith angles along the plane that contains the incident vector and surface normal vector. Incidence vector is given by solar geometry while the reflected is given by satellite view geometry, which is fixed for a geostationary satellite for any point in Earth's surface. For a combined assessment of these geometries, we plotted the analemma for 9 h, 10 h, and 11 h LT for the SIMA buoy coordinates (Table 2) at Serra da Mesa reservoir in Figure A3. Satellite viewing geometry (zenith and azimuth angles) was extracted from GOES-16 raw navigation files and plotted over. The analemma curve shows the sun position (elevation and azimuth) at the same hour throughout the year.

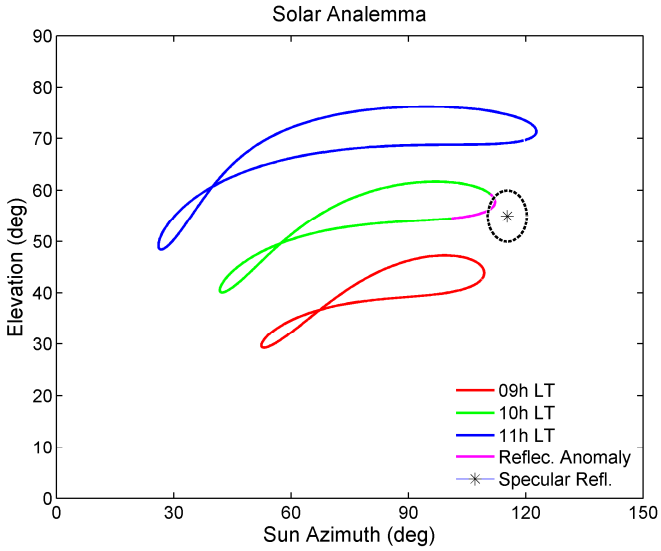

Figure A3. Analemma for 9 h (red), 10 h (green), and 11 h (blue) LT at Serra da Mesa reservoir (SIMA buoy coordinates) and corresponding specular reflection opposed to satellite viewing angles (black). Dash-dotted black line indicates a 5° margin from the specular position.

From Figure A3, it is possible to confirm that the reflectance anomaly observed during December and January at 10 h LT was caused by sun glint. Solar position cannot be treated as a point source. A margin of 5° from specular reflection position was included to account for angular variations due to sun disc solid angle (0.53°), lake extent, and mostly due to wavy water surface. This margin seems fairly conservative since any slope on the water facet causes a double deviation on a specular angle due to reflection symmetry. For oceans, where the water is far wavier, the sun glint is of greater concern and there is a well-established literature on its detection and correction [55,56]. For the work sequence, the 10 h LT samples affected by sun glint were excluded from the analysis.

References

1. Biggs, W.G.; Graves, M.E. A Lake Breeze Index. *J. Appl. Meteorol.* **1962**, *1*, 474–480. [CrossRef]
2. Rabin, R.M.; Stadler, S.; Wetzel, P.J.; Stensrud, D.J.; Gregory, M. Observed effects of landscape variability on convective clouds. *Bull. Am. Meteorol. Soc.* **1990**, *71*, 272–280. [CrossRef]
3. Segal, M.; Arritt, R.W.; Shen, J.; Anderson, C.; Leuthold, M. On the clearing of cumulus clouds downwind from lakes. *Mon. Weather Rev.* **1997**, *125*, 639–646. [CrossRef]
4. Asefi-Najafabady, S.; Knupp, K.; Mecikalski, J.R.; Welch, R.M.; Phillips, D. Ground-based measurements and dual-Doppler analysis of 3-D wind fields and atmospheric circulations induced by a meso-γ-scale inland lake. *J. Geophys. Res. Atmos.* **2010**, *115*. [CrossRef]
5. Iakunin, M.; Salgado, R.; Potes, M. Breeze effects at a large artificial lake: Summer case study. *Hydrol. Earth Syst. Sci.* **2018**, *22*, 5191–5210. [CrossRef]
6. Crosman, E.T.; Horel, J.D. Sea and Lake Breezes: A Review of Numerical Studies. *Bound. Layer Meteorol.* **2010**, *137*, 1–29. [CrossRef]
7. Maeda, E.E.; Ma, X.; Wagner, F.H.; Kim, H.; Oki, T.; Eamus, D.; Huete, A. Evapotranspiration seasonality across the Amazon Basin. *Earth Syst. Dyn.* **2017**, *8*, 439–454. [CrossRef]
8. Silva Dias, M.A.F.; Silva Dias, P.L.; Longo, M.; Fitzjarrald, D.R.; Denning, A.S. River breeze circulation in eastern Amazonia: Observations and modelling results. *Theor. Appl. Climatol.* **2004**, *78*, 111–121. [CrossRef]
9. Yin, X.; Nicholson, S.E.; Ba, M.B. On the diurnal cycle of cloudiness over Lake Victoria and its influence on evaporation from the lake. *Hydrol. Sci. J.* **2000**, *45*, 407–424. [CrossRef]
10. Stivari, S.M.S.; De Oliveira, A.P.; Karam, H.A.; Soares, J. Patterns of local circulation in the Itaipu Lake Area: Numerical simulations of lake breeze. *J. Appl. Meteorol.* **2003**, *42*, 37–50. [CrossRef]

11. Moura, M.A.L.; Meixner, F.X.; Trebs, I.; Lyra, R.F.D.F.; Andreae, M.O.; Nascimento Filho, M.F.D. Do Evidência observacional das brisas do lago de Balbina (Amazonas) e seus efeitos sobre a concentração do ozônio. *Acta Amaz.* **2004**, *34*, 605–611. [CrossRef]
12. Ackerman, S.A.; Heidinger, A.; Foster, M.J.; Maddux, B. Satellite Regional Cloud Climatology over the Great Lakes. *Remote Sens.* **2013**, *5*, 6223–6240. [CrossRef]
13. Assireu, A.T.; Pimenta, F.M.; Freitas, R.M. De Observações e modelagem da camada limite interna no entorno de extensos sistemas aquáticos. *Ciência Nat.* **2016**, *38*, 305. [CrossRef]
14. Ekhtiari, N.; Grossman-Clarke, S.; Koch, H.; de Souza, W.M.; Donner, R.V.; Volkholz, J. Effects of the Lake Sobradinho reservoir (Northeastern Brazil) on the regional climate. *Climate* **2017**, *5*, 50. [CrossRef]
15. Stivari, S.M.S.; De Oliveira, A.P.; Soares, J. On the climate impact of the local circulation in the Itaipu Lake area. *Clim. Chang.* **2005**, *72*, 103–121. [CrossRef]
16. Peel, M.C.; Finlayson, B.L.; McMahon, T.A. Updated world map of the Köppen-Geiger climate classification. *Hydrol. Earth Syst. Sci.* **2007**, *11*, 1633–1644. [CrossRef]
17. Diniz, F.D.A.; Ramos, A.M.; Rebello, E.R.G. Brazilian climate normals for 1981–2010. *Pesqui. Agropecuária Bras.* **2018**, *53*, 131–143. [CrossRef]
18. Vera, C.; Higgins, W.; Amador, J.; Ambrizzi, T.; Garreaud, R.; Gochis, D.; Gutzler, D.; Lettenmaier, D.; Marengo, J.; Mechoso, C.R.; et al. Toward a unified view of the American monsoon systems. *J. Clim.* **2006**, *19*, 4977–5000. [CrossRef]
19. Stech, J.L.; Lima, I.B.T.; Novo, E.M.L.M.; Silva, C.M.; Assireu, A.T.; Lorenzzetti, J.A.; Carvalho, J.C.; Barbosa, C.C.; Rosa, R.R. Telemetric monitoring system for meteorological and limnological data acquisition. *SIL Proc. 1922–2010* **2006**, *29*, 1747–1750. [CrossRef]
20. OSCAR—Observing Systems Capability Analysis and Review Tool. Available online: https://www.wmo-sat.info/oscar/satellites (accessed on 10 January 2020).
21. Moser, W.; Raschke, E. Incident Solar Radiation over Europe estimated from METEOSAT data. *J. Clim. Appl. Meteorol.* **1984**, *26*, 166–170. [CrossRef]
22. Stuhlmann, R.; Rieland, M.; Raschke, E. An improvement of the IGMK model to derive total and diffuse solar radiation at the surface from satellite data. *J. Appl. Meteorol.* **1990**, *29*, 586–603. [CrossRef]
23. Knapp, K.R. Scientific data stewardship of international satellite cloud climatology project B1 global geostationary observations. *J. Appl. Remote Sens.* **2008**, *2*, 23548. [CrossRef]
24. Rossow, W.B.; Walker, A.W.; Beushebel, D.; Roiter, M. *International Satellite Cloud Climatology Project (ISCCP): Description of New Cloud Datasets*; WMO/TD737; World Climate Research Programme (ICSU and WMO): Geneva, Switzerland, 1996; Volume 115.
25. Kidder, S.Q.; Haar, T.H.V. Clouds and aerosols. In *Satellite Meteorology*; Gulf Professional Publishing: Houston, TX, USA, 1995; pp. 259–305. [CrossRef]
26. Rossow, W.B.; Garder, L.C. Cloud detection using satellite measurements of infrared and visible radiances for ISCCP. *J. Clim.* **1993**, *6*, 2341–2369. [CrossRef]
27. Bottino, M.J.; Ceballos, J.C. Daytime cloud classification over South American region using multispectral GOES-8 imagery. *Int. J. Remote Sens.* **2015**, *36*, 1–19. [CrossRef]
28. Espinar, B.; Ramírez, L.; Drews, A.; Beyer, H.G.; Zarzalejo, L.F.; Polo, J.; Martín, L. Analysis of different comparison parameters applied to solar radiation data from satellite and German radiometric stations. *Sol. Energy* **2009**, *83*, 118–125. [CrossRef]
29. Samuelsson, P.; Tjernström, M. Mesoscale flow modification induced by land-lake surface temperature and roughness differences. *J. Geophys. Res. Atmos.* **2001**, *106*, 12419–12435. [CrossRef]
30. Segal, M.; Arritt, R.W. Nonclassical mesoscale circulations caused by surface sensible heat- flux gradients. *Bull. Am. Meteorol. Soc.* **1992**, *73*, 1593–1604. [CrossRef]
31. Doran, J.C.; Shaw, W.J.; Hubbe, J.M. Boundary layer characteristics over areas of inhomogeneous surface fluxes. *J. Appl. Meteorol.* **1995**, *34*, 559–571. [CrossRef]
32. Beyer, H.G.; Pereira, E.B.; Martins, F.R.; Abreu, S.L. Assessing satellite derived irradiance information for South America within the UNEP resource assessment project SWERA. In Proceedings of the 5th EuroSun, Freiburg, Germany, 20–23 June 2004; pp. 3–771.
33. Martins, F.R.; Pereira, E.B.; Silva, S.A.B.; Abreu, S.L.; Colle, S. Solar energy scenarios in Brazil, Part one: Resource assessment. *Energy Policy* **2008**, *36*, 2853–2864. [CrossRef]

34. Cano, D.; Monget, J.M.; Albuisson, M.; Guillard, H.; Regas, N.; Wald, L. A method for the determination of the global solar radiation from meteorological satellite data. *Sol. Energy* **1986**, *37*, 31–39. [CrossRef]
35. Dagestad, K.F.; Olseth, J.A. A modified algorithm for calculating the cloud index. *Sol. Energy* **2007**, *81*, 280–289. [CrossRef]
36. Bischoff-Gauß, I.; Kalthoff, N.; Fiebig-Wittmaack, M. The influence of a storage lake in the Arid Elqui Valley in Chile on local climate. *Theor. Appl. Climatol.* **2006**, *85*, 227–241. [CrossRef]
37. Thiery, W.; Martynov, A.; Darchambeau, F.; Descy, J.P.; Plisnier, P.D.; Sushama, L.; Van Lipzig, N.P.M. Understanding the performance of the FLake model over two African Great Lakes. *Geosci. Model. Dev.* **2014**, *7*, 317–337. [CrossRef]
38. Potes, M.; Salgado, R.; Costa, M.J.; Morais, M.; Bortoli, D.; Kostadinov, I.; Mammarella, I. Lake-atmosphere interactions at Alqueva reservoir: A case study in the summer of 2014. *Tellus Ser. A Dyn. Meteorol. Oceanogr.* **2017**, *69*, 1272787. [CrossRef]
39. Sills, D.M.L.; Brook, J.R.; Levy, I.; Makar, P.A.; Zhang, J.; Taylor, P.A. Lake breezes in the southern Great Lakes region and their influence during BAQS-Met 2007. *Atmos. Chem. Phys.* **2011**, *11*, 7955–7973. [CrossRef]
40. Physick, W. Numerical model of the sea-breeze phenomenon over a lake or gulf. *J. Atmos. Sci.* **1976**, *33*, 2107–2135. [CrossRef]
41. Estoque, M.A. Further Studies of a Lake Breeze Part 1: Observational Studies. *Mon. Weather Rev.* **1980**, *109*, 611–618. [CrossRef]
42. Corner, N.T.; McKendry, I.G. Observations and numerical modelling of lake Ontario breezes. *Atmos. Ocean* **1993**, *31*, 481–499. [CrossRef]
43. Miranda, A.C.; Miranda, H.S.; Lloyd, J.; Grace, J.; Francey, R.J.; Mcintyre, J.A.; Meir, P.; Riggan, P.; Lockwood, R.; Brass, J. Fluxes of carbon, water and energy over Brazilian cerrado: An analysis using eddy covariance and stable isotopes. *Plant Cell Environ.* **1997**, *20*, 315–328. [CrossRef]
44. Lorenzzetti, J.A.; Araújo, C.A.S.; Curtarelli, M.P. Mean diel variability of surface energy fluxes over Manso Reservoir. *Inland Waters* **2015**, *5*, 155–172. [CrossRef]
45. Bechtold, P.; Pinty, J.P.; Mascart, P. A numerical investigation of the influence of large-scale winds on sea-breeze- and inland-breeze-type circulations. *J. Appl. Meteorol.* **1991**, *30*, 1268–1279. [CrossRef]
46. Arritt, R.W. Effects of the large-scale flow on characteristic features of the sea breeze. *J. Appl. Meteorol.* **1993**, *32*, 116–125. [CrossRef]
47. Simpson, J.E. *Sea Breeze and Local Wind*; Cambridge University Press: New York, NY, USA, 1994; p. 252.
48. King, P.W.S.; Leduc, M.J.; Sills, D.M.L.; Donaldson, N.R.; Hudak, D.R.; Joe, P.; Murphy, B.P. Lake breezes in southern Ontario and their relation to tornado climatology. *Weather Forecast.* **2003**, *18*, 795–807. [CrossRef]
49. Physick, W.L. Numerical experiments on the inland penetration of the sea breeze. *Q. J. R. Meteorol. Soc.* **1980**, *106*, 735–746. [CrossRef]
50. Evan, A.T.; Heidinger, A.K.; Vimont, D.J. Arguments against a physical long-term trend in global ISCCP cloud amounts. *Geophys. Res. Lett.* **2007**, *34*, L04701. [CrossRef]
51. Garratt, J.R. Review: The atmospheric boundary layer. *Earth Sci. Rev.* **1994**, *37*, 89–134. [CrossRef]
52. McGill, R.; Tukey, J.W.; Larsen, W.A. Variations of box plots. *Am. Stat.* **1978**, *32*, 12–16. [CrossRef]
53. Pereira, E.B.; Martins, F.R.; Gonçalves, A.R.; Costa, R.S.; Abreu, S.L.; Ruther, R.; Lima, F.J.L.; Pereira, S.V.; Souza, J.G. *Atlas Brasileiro de Energia Solar*, 2nd ed.; INPE: Sao Jose dos Campos, Brazil, 2017; ISBN 978-85-17-00090-4.
54. Rosa-Clot, M.; Tina, G.M. *Submerged and Floating Photovoltaic Systems: Modelling, Design and Case Studies*; Academic Press: Cambridge, MA, USA, 2017; ISBN 9780128123232.
55. Kay, S.; Hedley, J.D.; Lavender, S. Sun glint correction of high and low spatial resolution images of aquatic scenes: A review of methods for visible and near-infrared wavelengths. *Remote Sens.* **2009**, *1*, 697–730. [CrossRef]
56. Zhang, H.; Wang, M. Evaluation of sun glint models using MODIS measurements. *J. Quant. Spectrosc. Radiat. Transf.* **2010**, *111*, 492–506. [CrossRef]